Feature Detection With a Constant FAR in Sparse 3-D Point Cloud Data

Daniel Lühr, *Senior Member, IEEE*, Martin Adams, *Senior Member, IEEE*, Hamidreza Houshiar, Dorit Borrmann, and Andreas Nüchter, *Member, IEEE*

Abstract— The detection of markers or reflectors within point cloud data (PCD) is often used for 3-D scan registration, mapping, and 3-D environmental modeling. However, the reliable detection of such artifacts is diminished when PCD is sparse and corrupted by detection and spatial errors, for example, when the sensing environment is contaminated by high dust levels, such as in mines. In the radar literature, constant false alarm rate (CFAR) processors provide solutions for extracting features within noisy data; however, their direct application to sparse, 3-D PCD is limited due to the difficulty in defining a suitable noise window. Therefore, in this article, CFAR detectors are derived, which are capable of processing a 2-D projected version of the 3-D PCD or which can directly process the 3-D PCD itself. Comparisons of their robustness, with respect to data sparsity, are made with various state-of-the-art feature detection methods, such as the Canny edge detector and random sampling consensus (RANSAC) shape detection methods.

Index Terms— Constant false alarm rate (CFAR), feature detection, point cloud data (PCD), radar.

I. Introduction

APPLICATIONS such as image alignment, tracking moving objects in a scene, and ladar surveying involve the use of sensors to monitor the environment. They belong to research fields as diverse as remote sensing, computer vision, medical imaging, augmented reality, and robotic mapping. It is usually necessary to match and align successive scans from the environment, often from different relative locations. In some appli-

cations, this process is referred to as registration, examples of which include point-based registration techniques, such as the iterative closest point (ICP) method [1]. Some of the limitations and difficulties of registration approaches, particularly in the application of airborne laser scanning, are presented in [2].

In several applications, control points are needed to identify the same part of an object within the different datasets. Regardless of the application, the general procedure to obtain such control points is similar. This involves the detection of some identifiable features of the objects in each dataset and matching the detected features of the corresponding objects across the different datasets. If the measured objects exhibit some unique characteristic, which can be used for identification, this feature is usually calculated or "extracted" directly from the dataset. Methods to extract such features include the scale-invariant feature transform (SIFT) [3], speeded up robust features (SURFs) [4], Oriented features from accelerated segment test (FAST) and rotated Binary robust independent elementary features (BRIEFs) (ORB) [5], Canny edge detection [6], [7], random sampling consensus (RANSAC) shape detection [8], [9], and surface normal features used in 2-D or 3-D [10] image processing [3], [5], [11], [12]. Customized feature detection methods also exist, such as [13], in which street light poles are detected from LiDAR point cloud data (PCD) in a semiautomated manner.

Some environments lack the number or quality of natural features needed to achieve a required level of accuracy. An example includes terrain laser scanning (TLS) in a forest environment [14]. Also, the environment may be highly dynamic, thus altering the potential natural features from scan to scan. In these situations, the use of artificial landmarks is preferable.

When the objects lack an identifiable characteristic, artificial markers can be added to the observed objects. Depending on the marker's distinguishable information, which can be shape, reflectivity, color, pattern, texture, or local gradient, different methods for detecting these features should be used. Often, combinations of these characteristics are exploited simultaneously [15], [16].

Some standard automated procedures to detect artificial markers are template matching, image segmentation, and edge detection [17]. It will be shown, in this article, that the nature of 3-D PCD can negatively impact the performance of these techniques, motivating the need for automatic feature extraction dedicated to 3-D PCD.

Automatic methods for detecting reflective markers with 3-D laser range scanners are presented here. These approaches are based on the adaptive threshold obtained by using constant false alarm rate (CFAR) processors, which are used to segment the markers from the rest of the data. CFAR processors are well known in the radar community and are capable of feature/target detection at low signal-to-noise ratios (SNRs), achieving high probabilities of detection while bounding the false alarm rate (FAR). They have been applied to many diverse areas in the literature. For example, a CFAR edge detector for polarimetric synthetic aperture radar (SAR) data is presented in [18]. This detector overcomes the limitations of standard edge detection methods used with optical images since it is adapted for SAR image statistics (i.e., the speckle distribution). Furthermore, this method is capable of using the full polarimetric information, unlike other CFAR detectors developed for SAR data, by developing a new test for the SAR data complex covariance matrix, which follows a Wishart distribution. Also, a robust CFAR detector based on truncated statistics developed for ship detection in SAR data is described and compared to other approaches in [19] and [20]. This method shows improved detection in high-density multitarget situations. CFAR-based methods have also been used with other sensors. One such application consists of an image processing technique to detect electrical lines in laser range finder images [21]. CFAR methods have also been used to detect and track dim points with low SNR in infrared image (IR) sequences [22].

The methods of automatically detecting reflectors in clutter presented in this article use the intensity level of energy reflected by markers in 3-D PCD. Range information is also incorporated to calculate an adaptive threshold, motivated by the results obtained in [21]. Classical CFAR methods are adapted to disambiguate the reflective markers from the rest of the objects in the ladar images. These stochastic methods are designed to keep the FAR at a predetermined (preferably low) constant level, and they exhibit a relatively low computational complexity with respect to other detection methods [22].

The proposed methods also estimate the probability of detection for each point, serving as a measure of how likely that point corresponds to an actual marker. This can be used by automatic registration systems to give higher weights to the markers with higher detection rates.

Specifically, in this article, standard cell averaging (CA) and ordered statistics (OS) CFAR processors are applied to 3-D laser PCD, using both its raw 3-D format and its 2-D projections. Both CA-CFAR and OS-CFAR processors are chosen since it is documented that CA-CFAR performance is good when homogeneous clutter can be assumed [23]. This means that the clutter is assumed to follow a Weibull distribution. On the other hand, in the case of nonhomogeneous clutter, OS-CFAR processors have been shown to yield superior performance. Nonhomogeneous clutter corresponds to clutter that follows a Weibull amplitude distribution with parameters that change abruptly as a function of range [23]. The contributions include the following.

1) Adaptive, parametric CFAR detectors, capable of utilizing 3-D power and range information from PCD when projected into 2-D. Range information is used to automatically adjust the 2-D CFAR window size and, hence, number of the guard and reference cells, yielding adaptive 2-D CFAR processors capable of achieving higher detection probabilities than their nonadaptive counterparts.

2) Modified CFAR algorithms, for direct application to sparse, 3-D PCD.

Three standard semantic feature detection methods are used for benchmark comparisons: 1) constant threshold segmentation [24]; 2) RANSAC shape detection [8] (both methods used in both 2-D and 3-D representations); and 3) Canny edge detection [6], [7] (for 2-D projected data). All the methods are followed by a standard connected component analysis (CCA) [24] to identify and label the detected areas (2-D data) or volumes (3-D data).

After applying the derived 2-D and 3-D CFAR processors, as well as the above benchmark detection algorithms, comparative results in the form of receiver operating characteristics (ROC) curves are shown. These are based on the standard definitions of true positive rate (TPR) versus actual FAR.

II. FEATURE DETECTION WITH 3-D PCD—THE SPARSITY PROBLEM

As a 3-D sensor scans the environment, space is discretized in 3-D, typically in the range r, bearing angle ϕ, and elevation angle θ space - i.e., into polar voxels. In addition to spatial information, many sensors also record reflected intensity or received power and have their own detection electronics. Such sensors only report the received power within polar voxels in which detections are made, leaving all other voxels void of such information. The set of voxels corresponding to detections, and hence containing received power information, comprises the PCD. Thus, if the spherical space within the sensor's field of view is considered to be a 3-D matrix containing cells that provide sufficient reflective intensity, then, not all elements of the matrix have a value. Such a data matrix is considered to be sparse. This is an advantage from the point of view of data size because sensors, such as laser range finders, can achieve a very high resolution, producing millions of points in a point cloud. However, because of this sparsity, 3-D PCD cannot be processed in the same way as 1-D signals, 2-D images, video, and some 3-D data that are represented by dense matrices. As discussed in Section IV, data processing methods need to be adapted for direct use with PCD. Alternatively, a projected 2-D image obtained from the PCD can also be used, but the sparsity is also transferred to the 2-D representation, which then causes problems with 2-D image processing algorithms. In spherical coordinates, as the range to points increases, the voxel volume representing a particular point increases together with the distance between "adjacent" points (i.e., adjacent voxels). Therefore, some of the difficulties arising from the nature of 3-D PCD are as follows.

1) When the 3-D data are projected to a 2-D image, targets at different ranges from the sensor appear to have different sizes. Also, if the sensor is not oriented along the line of sight of the target's surface normal, its shape will be distorted.

2) In both 3-D or 2-D projected data, some nontarget objects might present a similar reflected intensity as the

targets themselves, which can confuse threshold detectors. In this case, usually, a second detector is used to discard false positives, such as a shape or size detector. The sparsity of the data, however, can affect the results of these methods. For example, discontinuities in the pixels' (in 2-D projected data) or points' (in 3-D data) intensity values will cause size or shape detectors to fail. Also, edge detectors are affected by this phenomenon as false edges arise at these discontinuities, which can be misinterpreted as actual targets.

The proposed detection methods, in this article, have been modified to cope with these problems.

III. OVERVIEW OF CFAR PROCESSORS

Before presenting the adaptation of the CFAR concepts to the problem, a brief overview of CFAR methods is now given.

The CFAR concept refers to a family of adaptive algorithms widely used in radar to detect target returns against a background of noise and clutter. The starting point for the processing of radar data is the standard assumption that the target absence and presence distribution types are known, but not their moments, since these typically vary and should be estimated. In this case, a test statistic must be derived. If such a statistic can be found, which is independent of any unknowns, then the detection method is known as a CFAR detector.

In most radar signal processing literature to date, a CA-CFAR detector is the preferred method of target detection [25], [26].

1) CA-CFAR: An adaptive threshold $S^{\text{CA-CFAR}}$ necessary for CA-CFAR-based detection is determined as follows. Reference [27] shows that the detection probability of a Rayleigh fluctuating target, embedded in exponential noise or clutter, can be determined from the CA-CFAR parameters

$$P_D^{\text{CA-CFAR}}(q) = \left[1 + \frac{\tau^{\text{CA-CFAR}}}{W_f} \left(\frac{1}{1 + \widehat{\eta}^{\text{SNP}}(\text{CUT})} \right) \right]^{-W_f} \tag{1}$$

where W_f is the size of the CFAR window and $\tau^{\text{CA-CFAR}}$ is defined as

$$\tau^{\text{CA-CFAR}} = W_f \left(\left(P_{\text{fa}}^{\text{CA-CFAR}} \right)^{\frac{-1}{W_f}} - 1 \right) \tag{2}$$

where $P_{\text{fa}}^{\text{CA-CFAR}}$ is the chosen, acceptable false alarm probability and $\widehat{\eta}^{\text{SNP}}(\text{CUT})$ is the estimated received SNP in the cell under test (CUT), calculated as

$$\widehat{\eta}^{\text{SNP}}(\text{CUT}) = \frac{P_{\text{CUT}}}{T_{\text{CUT}}^{\text{CA-CFAR}}} \tag{3}$$

where P_{CUT} is the received power from the radar in the CUT. $T_{\text{CUT}}^{\text{CA-CFAR}}$ is the test statistic derived from power values in the neighborhood of the CUT. In the case of the CA-CFAR detector, $T_{\text{CUT}}^{\text{CA-CFAR}}$ is the average power value recorded in the vicinity of the CUT. The adaptive threshold at the CUT is then defined as

$$S^{\text{CA-CFAR}}(\text{CUT}) = \tau^{\text{CA-CFAR}} \, T_{\text{CUT}}^{\text{CA-CFAR}}. \tag{4}$$

Hence, for chosen values of W_f and $P_{\text{fa}}^{\text{CA-CFAR}}$, the detection probability $P_D^{\text{CA-CFAR}}$ of a target, as a function of the
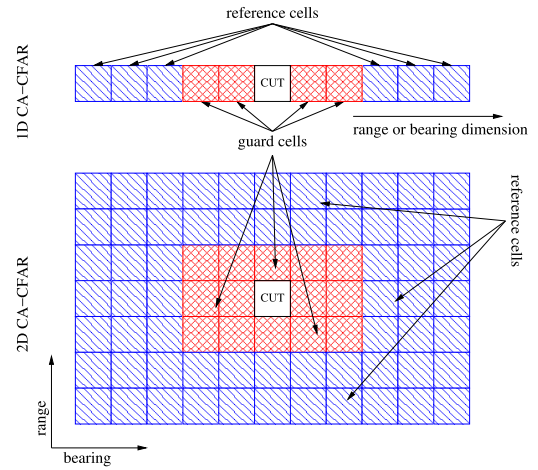

Fig. 1. 1-D and 2-D CA-CFAR reference windows.

estimated received SNP $\widehat{\eta}^{\text{SNP}}$, is given by (1). In general, in order to assure that the cells in the window contain noise information only, "guard cells" are selected around the CUT, accounting for the fact that some target power spreads to adjacent cells of the CUT.

In the case of scanning sensors, the above-mentioned analysis can be extended to 2-D to process the range and bearing dimensions simultaneously, thus jointly analyzing all available information. The 1-D window used to estimate the test statistic is extended to a 2-D area surrounding the CUT, as shown in Fig. 1. It has been shown that for a given window size in range and bearing and a chosen false alarm probability $P_{\text{fa}}^{\text{CA-CFAR}}$, the 2-D CA-CFAR probability of detection is higher than its 1-D equivalent, for all received signal to noise power ratios η^{SNP} [28].

2) OS-CFAR: Several other CFAR methods have been developed, such as the OS-CFAR processor, which has been reported to perform well for large targets (with respect to the spatial resolution) and in SAR images with the higher effect of multiplicative speckle noise present in such images [23]. In the OS-CFAR detector, the equivalent test statistic $T_{\text{CUT}}^{\text{OS-CFAR}}$ is obtained by choosing the kth value from the ordered set of power values in the CFAR window surrounding the CUT as follows [29]:

$$S_{(1)} \leq S_{(2)} \leq \cdots \leq S_{(k)} \leq \cdots \leq S_{(W_f-1)} \leq S_{(W_f)}. \tag{5}$$

A value of $k = (3\,W_f/4)$ has been suggested in [23] to represent a good estimate for typical radar applications. The parameter $\tau^{\text{OS-CFAR}}$ is calculated numerically from

$$P_{\text{fa}}^{\text{OS-CFAR}} = \prod_{i=0}^{k-1} \frac{W_f - i}{W_f - i + \tau^{\text{OS-CFAR}}} \tag{6}$$

while the probability of detection is obtained from

$$P_D^{\text{OS-CFAR}} = \prod_{i=0}^{k-1} \frac{W_f - i}{W_f - i + \frac{\tau^{\text{OS-CFAR}}}{1 + \widehat{\eta}^{\text{SNP}}(q)}}. \tag{7}$$

$\tau^{\text{OS-CFAR}}$ is determined numerically from (6) according to the chosen acceptable probability of false alarm $P_{\text{fa}}^{\text{OS-CFAR}}$.

Similarly to the CA-CFAR processor, the OS-CFAR adaptive threshold is

$$S^{\text{OS-CFAR}}(\text{CUT}) = \tau^{\text{OS-CFAR}} \, T_{\text{CUT}}^{\text{OS-CFAR}} \qquad (8)$$

and the resulting detection probability is given by (7).

IV. ADAPTATION OF CFAR ALGORITHMS TO 3-D PCD

The 3-D sensor type addressed in this article yields spherical coordinate information (r, θ, ϕ) and a value for the received reflected intensity. In order to use the CFAR methods with 3-D data, two approaches are proposed. The first one is to project the 3-D data onto a 2-D image and then apply 2-D CFAR methods. This is a common approach to visualize 3-D data (e.g., cartographic maps and ladar scenes). Although there are many mature, robust, and fast algorithms to process 2-D data, all projection techniques distort the spatial relations of objects in the original image, leading to performance detriments. Thus, a second alternative is to apply the CFAR techniques directly onto the undistorted 3-D data. Often, 3-D algorithms are less developed than their 2-D counterparts and usually slower due to the higher amount of data to be processed.

Standard CA-CFAR, OS-CFAR, or other CFAR methods suitable for 2-D data can be directly applied to the ladar intensity image, in the same way they are used with radar data. The standard CFAR methods will be used as benchmarks to compare the performance of the two CFAR extensions proposed in this article, both of which aim at incorporating range and reflectance information simultaneously into the CFAR analysis. The performance of the CFAR methods is expected to improve when using range information. The first algorithm corresponds to an adaptive CFAR method that uses range information to adapt the size of the reference and guard cell windows. The second proposed variation corresponds to a direct CFAR implementation in 3-D space. These two approaches are analyzed in Sections IV-A and IV-B respectively.

A. Projecting 3-D Range and Intensity Information Into 2-D Images for Feature Detection

In this approach, 3-D intensity values are projected onto a 2-D image using bearing and elevation angle values. Instead of intensity values, range information can also be projected using a similar transformation. This approach has the drawback that any projection transform introduces distortions, which affects the shape of features/markers and, consequently, detriments their detection. Also, areas of the image with no intensity/range data should be replaced with "appropriate values," which are usually maximum range/minimum intensity values, to avoid false detections. A thorough analysis of various projections and their effects in feature-based detectors in 3-D ladar applications is given in [30]. Two of the projections presented in [30] will be used here. The first is the equirectangular projection because it is the simplest and the most widely used projection in image processing. The other is the Mercator projection, which is mainly used in cartography and geoinformatics. This projection was shown in [30] to outperform other projections for 3-D laser surveying,

TABLE I
SUMMARY OF PROJECTIONS USED

Projection	$f_x(\theta, \phi)$	$f_y(\theta, \phi)$	hor. FoV	vert. FoV
Equirect.	θ	ϕ	360°	180°
Mercator	θ	$\ln\left(\tan\phi + \frac{1}{\cos\phi}\right)$	360°	150°

by achieving high registration rates in various indoor and outdoor environments as well as for different combinations of descriptors and feature detectors, such as SIFT, SURF, ORB, and FAST. This projection also has the capability of processing full 360° panoramic images.

In general, projecting 3-D data onto a 2-D image requires the mapping of the r, θ, ϕ coordinates to 2-D x, y coordinates. In equirectangular projection, the bearing and elevation angles are directly mapped to horizontal and vertical coordinates of a grid without any transformation or scaling. As a result, vertical straight lines in 3-D space remain as vertical straight lines in the 2-D image, but, with the exception of the horizon, the horizontal straight lines become curves. Also, the poles in 3-D are stretched to the entire width of the 2-D image at the top and bottom edges.

Mercator projection presents less distortion than equirectangular projection and suffers less vertical stretching. Table I summarizes these two projections [30]. Once intensity data have been projected into a 2-D image, standard CFAR processors can be applied to obtain the adaptive CFAR thresholds.

1) 2-D Adaptive Window CFAR Detection: Intensity and range data can also be combined to increase the probability of detection of 2-D CFAR processors. This work proposes the use of range information to adjust the size of the CFAR window to match the expected size of the markers, which results in a CFAR processor with adaptive window size, number of guard cells, and $\tau^{\text{CA-CFAR}}$ (or $\tau^{\text{OS-CFAR}}$) parameters.

For each CUT, the range information is used to calculate the appropriate sizes of the reference and guard windows in the projected bearing-elevation space. By matching the expected size of the markers to the guard cells window, the reference cells' window would be assumed to contain only noise or clutter values.[1] Thus, the CFAR assumptions would be enforced, and the performance of the detector should be improved [23]. A description of this proposed method now follows.

Let $r_{\text{CUT}}, \theta_{\text{CUT}}$, and ϕ_{CUT} be the coordinates of the CUT in the original spherical coordinates. Also, let R_T be the assumed known effective radius of the marker, and if $\theta_T^+, \theta_T^-, \phi_T^+$, and ϕ_T^- represent the border angles of the marker in the original space (see Fig. 2), then

$$\theta_T^+ = \theta_{\text{CUT}} + R_T/r_{\text{CUT}}, \quad \theta_T^- = \theta_{\text{CUT}} - R_T/r_{\text{CUT}} \quad (9)$$
$$\phi_T^+ = \phi_{\text{CUT}} + R_T/r_{\text{CUT}}, \quad \phi_T^- = \phi_{\text{CUT}} - R_T/r_{\text{CUT}} \quad (10)$$

where the small angle assumption has been applied to $\theta_T^+ - \theta$, $\theta - \theta_T^-$, $\phi_T^+ - \phi$, and $\phi - \phi_T^-$ since the diameter of the markers is usually much smaller than their distance from the sensor.

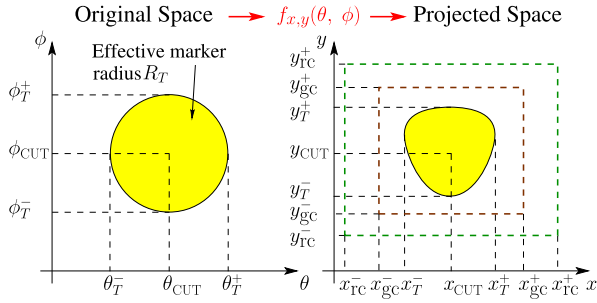[1]Assuming that no other markers are in the vicinity of the CUT.

Fig. 2.   Adaptive 2-D-CFAR and its parameters.

Also, if $f_x(\theta, \phi)$ and $f_y(\theta, \phi)$ are the transform functions from the original to the projected space, as defined in Table I, then the region W_T corresponding to the marker in the original space and the region W'_T to that in the projected space are defined as

$$W_T = \left\{ (\theta_T, \phi_T) \,\middle|\, \sqrt{\theta^2 + \phi^2} \leq \frac{R_T}{r_{\text{CUT}}} \right\} \tag{11}$$

$$W'_T = \{(f_x(\theta, \phi), f_y(\theta, \phi)) \mid (\theta, \phi) \in W_T\} \tag{12}$$

where W_T is the set of angle pairs in the original space, while W'_T is the set of (x, y) coordinates in the projected space, defined in formal set builder notation [31]. The bounding coordinates of the projected marker are given by

$$x_T^+ = \max_{(\theta, \phi) \in W_T} (f_x(\theta, \phi)), \quad x_T^- = \min_{(\theta, \phi) \in W_T} (f_x(\theta, \phi)) \tag{13}$$

$$y_T^+ = \max_{(\theta, \phi) \in W_T} (f_y(\theta, \phi)), \quad y_T^- = \min_{(\theta, \phi) \in W_T} (f_y(\theta, \phi)). \tag{14}$$

In the following, the subscripts "gc" and "rc" will refer to guard cells and reference cells, respectively. CFAR guard and reference cell windows in the projected space are then defined as

$$W'_{\text{gc}} = \left\{ (x, y) \mid \left(a x_T^- < x < a x_T^+\right) \wedge \left(a y_T^- < y < a y_T^+\right) \right\} \tag{15}$$

$$W'_{\text{rc}} = \left\{ (x, y) \mid \left(b x_T^- < x < b x_T^+\right) \wedge \left(b y_T^- < y < b y_T^+\right) \right.$$
$$\left. \wedge (x, y) \notin W'_{\text{gc}} \right\} \tag{16}$$

where the guard cell window in the projected space W'_{gc} is a rectangle, which encompasses a scaled version of the projected marker image. The scale used for W'_{gc} is a ($a > 1$), and the scale used for W'_{rc} is b ($b > a$).

In standard CFAR methods, the window width ($\Delta x_\pi = x_\pi^+ - x_\pi^-$) and height ($\Delta y_\pi = y_\pi^+ - y_\pi^-$), with $\pi \in \{\text{gc}, \text{rc}\}$, are fixed parameters in the projected space coordinates. On the other hand, the proposed adaptive algorithm uses R_T as a parameter and the measured range r_{CUT} to calculate the window widths and heights in the projected space for each CUT, using (11)–(16). The guard cell window width and height are calculated such that W'_{gc} includes the whole W'_T region. This is achieved by iteratively growing the window in the projected space and calculating the window size in the original space until the desired size of the marker is reached, for each CUT. The reference window width and height, on the other hand, are chosen such that the
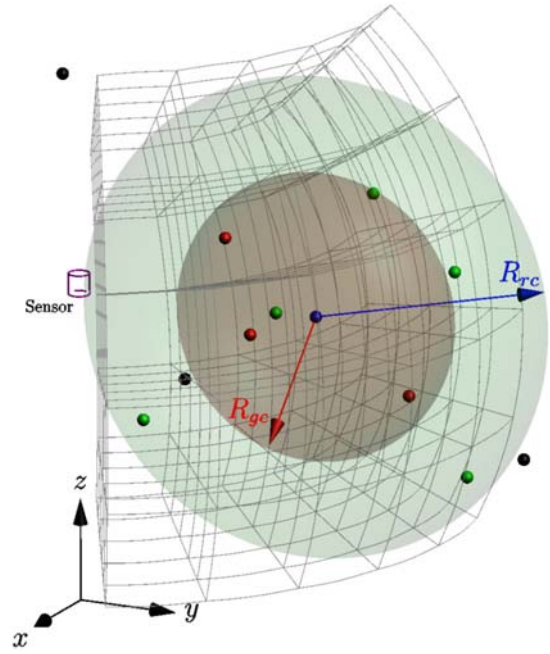

Fig. 3.   CFAR windows in 3-D space. Blue point: point in CUT. Red points: points within the guard window (brown sphere). Green points: points within the reference window (the green region outside of guard window). Black points: points outside the reference window and not considered in CFAR calculations.

window is larger than the guard window and large enough to obtain a representative estimate of the noise power while, at the same time, not so large that it would include other markers. Due to computational constraints, it is also desirable to keep the reference window to a limited size.

The thresholds, $\tau^{\text{CA-CFAR}}$ (2) and $\tau^{\text{OS-CFAR}}$ (determined from (6)), and the test statistics, $T_{\text{CUT}}^{\text{CA-CFAR}}$ and $T_{\text{CUT}}^{\text{OS-CFAR}}$, are then calculated using these reference and guard cell windows and assigned to each CUT. The adaptive CFAR thresholds, $S^{\text{CA-CFAR}}(\text{CUT})$ and $S^{\text{OS-CFAR}}(\text{CUT})$, are then calculated from (4) and (8).

B. Direct CFAR Detection in 3-D Space

The second approach is to directly apply a 3-D CA-CFAR processor to the intensity information in the 3-D PCD. The 3-D range, bearing, and elevation coordinates are first converted to x, y, z coordinates in the Cartesian space. This has the advantage of not having the distortions introduced by the projections. On the other hand, special considerations need to be taken to apply the CFAR algorithms to sparse 3-D data. To illustrate the proposed approach, Fig. 3 shows 3-D CFAR windows operating on 3-D PCD. The 3-D CFAR algorithm discretizes the space into 3-D voxels (cells) corresponding to range, bearing, and elevation bins, represented by the gray framed voxels. The algorithm iterates over all 3-D data points in the point cloud. Each point falls inside a voxel (cell), which becomes the CUT once (blue point in Fig. 3). Then, all surrounding data points that fall into the guard window (brown sphere with radius R_{gc}) are ignored, while the data points in the reference window (green section of radius R_{rc}) are used to estimate the adaptive threshold. In the particular

case of the CA-CFAR processor, the average received power, $T_{\text{CUT}}^{\text{CA-CFAR}} = T_{\text{CUT}}^{\text{CA-CFAR-3D}}$ in the reference window, used to estimate the threshold, is

$$T_{\text{CUT}}^{\text{CA-CFAR-3D}} = \frac{1}{V_R} \sum_{\mathbf{x}_i \in R} I_{\mathbf{x}_i} \quad (17)$$

where $I_{\mathbf{x}_i}$ is the intensity value of data point $\mathbf{x}_i$, R represents the reference window, and V_R is the number of reference points in R. Analogously, the OS-CFAR detector's test statistic $T_{\text{CUT}}^{\text{OS-CFAR-3D}}$ is calculated by ordering all points in the reference window according to their power as in (5) and then selecting the kth value.

In 3-D space, the exact location of each measurement is used, while in the 2-D projections, usually, interpolation is used to assign measurements to pixels in the 2-D image grid from the 3-D data. Therefore, the direct application of a CFAR detector to 3-D PCD is expected to increase CFAR performance since no distortion of the shape and size of the markers occurs. State-of-the-art CFAR processors assume that none, or a relatively small amount, of the reference cells are part of the object being detected. Therefore, the volume of the guard cells window should be large enough to contain as many of a marker's cells as possible. Likewise, the reference window should be large enough to contain cells corresponding to noise and clutter to obtain a valid estimate of the noise power. Conversely, the reference window should not include target cells from a neighboring object.[2]

Unlike A-scope radar data or 2-D images, where contiguous cells usually have contiguous indexes, 3-D point clouds are often large, unstructured, lists of 3-D coordinates. Therefore, an efficient method to organize and search points in a multidimensional space is a k-d tree [32]. The nearest neighbor algorithm, which takes advantage of data structured in a k-d tree, is used to find the guard and reference cells. The implementation used in this work is based on the method described in [33].

Because of sparsity, there may be few points in the reference window. In this case, the test statistics, $T_{\text{CUT}}^{\text{CA-CFAR}}$ and $T_{\text{CUT}}^{\text{OS-CFAR}}$, give less reliable estimates of the noise power. When there are no points in the reference window, the noise estimate is undefined, and in this work, such CUTs are discarded.[3]

C. Benchmark Algorithms for Comparison

All the previously presented CFAR algorithms are compared with three state-of-the-art marker detection methods, namely, segmentation thresholding, Canny edge detection [7], and RANSAC shape detection [6], [8]. These algorithms are chosen since they can be designed to extract the reflector type markers examined in this article, either via their relative reflectivity, compared with their surroundings or their shape.

This is in contrast with other feature detection algorithms, such as ORB, SIFT, and SURF, that detect more complex image-based features, not necessarily directly related to the reflectors examined here.

1) RANSAC (RANSAC2D and RANSAC3D) Implementation: For benchmark comparisons, the "Scikit-image" implementation of RANSAC shape detection is applied to all of the projected 2-D images. Due to range errors and the projection distortions that result when converting the PCD into 2-D images, the disk-shaped reflectors do not always give perfect disks in their images, and therefore, the detection of ellipsoids proved more robust.

In the ensuing experiments, ROCs are produced by varying the detectors' false positive rates (FPRs). For the 2-D RANSAC Scikit-image approach (RANSAC2D), this was achieved by varying the residual threshold, which corresponds to the maximum distance for a data point to be classified as an inlier [6], [7].

In the 3-D PCD, a RANSAC implementation, which detected ellipsoids based on [34], was used to detect the disk-shaped reflectors. This is due to the foreshortening possible when scanning a circular disk. To vary the FPR for 3-D RANSAC ROC generation, the equivalent "max distance to primitive" parameter was varied in the "Cloudcompare tool" according to [34].

Due to the high resolution of the 3-D laser scanner, each target is represented by several points in the data set. In order to obtain a single detection per actual target, the connected component labeling algorithm is used to group points [24].

2) Canny Edge Detection (Canny) Implementation: The benchmark Canny edge detection approach adopted in the transformed 2-D images is taken from the OpenCV source libraries [35]. Once the image gradient magnitudes and directions are determined, the detector requires two image gradient thresholds. Edges with intensity gradient higher than the largest threshold are classified as edges, and those with intensity gradient lower than the smallest threshold are discarded. Edges with intensity gradient between the two thresholds are classified as edges based on their connectivity. This provides a form of hysteresis thresholding. In the Scikit image implementation [6], both thresholds are defined from a single parameter. In the benchmark Canny edge detector applied here, this single parameter was varied, which, in turn, varies both upper and lower gradient magnitude thresholds, which, in turn, varies the FPR of the Canny edge detector.

3) Segmentation Thresholding (cth2D and cth3D) Implementation: Segmentation thresholding uses an image intensity threshold to detect the reflective markers. Pixels with image intensities above the set threshold are assumed to correspond to the markers. To vary the FPR for the generation of the cth2D and cth3D ROCs, the segmentation threshold parameter is varied between the minimum image intensity to its maximum.

V. PCD-BASED CFAR EXPERIMENTS

In all the results presented in this section, the algorithms used for comparison are labeled Canny, cth, RANSAC, cacfar and oscfar corresponding to the Canny edge detector, segmentation thresholding, RANSAC and the newly developed

---

[2]The reference window should be smaller than the expected minimum distance between targets and should contain enough noise samples. In the experiments, reference cell window diameters 1.5 to 2.0 times larger than the corresponding guard cell window diameters gave satisfactory results.

[3]Note that an alternative method in this extreme case would be to use the received power from the spatially closest point as an estimate of the noise power, assuming that it is not another reflector.

TABLE II
CFAR PARAMETERS. PIXEL UNITS ARE LABELED px

Method	Parameter	Value	unit
ca/oscfar2Dstd	$\Delta x_{rc} = \Delta y_{rc}$	35	px
	$\Delta x_{gc} = \Delta y_{gc}$	10	px
ca/oscfar2Dadp	R_T	25	mm
	a	2	
	b	7	
ca/oscfar3D	$R_{rc}(= bR_T)$	175	mm
	$R_{gc}(= aR_T)$	50^4	mm

CA-CFAR and OS-CFAR algorithms, respectively. In addition, each label is appended with the tag 2-D or 3-D to differentiate the respective version. CFAR 2-D methods carry the suffix *std* to indicate the standard (fixed window size) version or *adp* to note the adaptive (adaptive window size) version.

The format of the results for all data sets consists of experimentally determined ROC curves, determined by varying the appropriate detection parameter for each algorithm. Correspondingly, in the derived CFAR methods, the theoretical FAR parameter was varied. These plots correspond to the TPR, determined by

$$\text{TPR} = \frac{\text{TP}}{\text{TP} + \text{FN}} = \frac{\text{No. correctly detected targets}}{\text{Real number of targets}} \quad (18)$$

where TP corresponds to the number of correct detections and FN corresponds to the number of missed detections, versus the actual FAR, determined by

$$\text{FAR} = \frac{\text{FP}}{\text{FP} + \text{TN}} = \frac{\text{No. false alarms}}{\text{Total no. non-target points}} \quad (19)$$

where FP corresponds to the number of false detections and TN corresponds to the number of points/pixels that do not correspond to targets.

For each data set, first, ROC curves are shown for the detectors applied directly to the 3-D PCD. This is followed by ROC plots for the detection methods adapted to process the projected 2-D versions of the 3-D PCD. Finally, the analysis of each data set yields plots of the true FAR versus the theoretical probability of false alarm parameter set in the CFAR algorithms. This is to give an indication of how well each detection algorithm achieves its theoretical FAR.

In all of the following results, the reference and guard window cell sizes are given in Table II.

A. Results With Simulated Data

The methods were first tested in a simulated environment. This allows tests under controlled detection statistics (clutter and detection probabilities) and knowledge of the ground-truth positions of the markers.

The simulated environment consists of four sets of five targets, with all five targets in each set presenting the same SNR, but different SNRs for each set. The five targets in

---

[4]Note that the diameter rather than the radius of the markers was used to set the guard window size, since the CUT could lie on or near the circumference of a marker. Hence $R_{gc} = aR_T$, with $a = 2$.
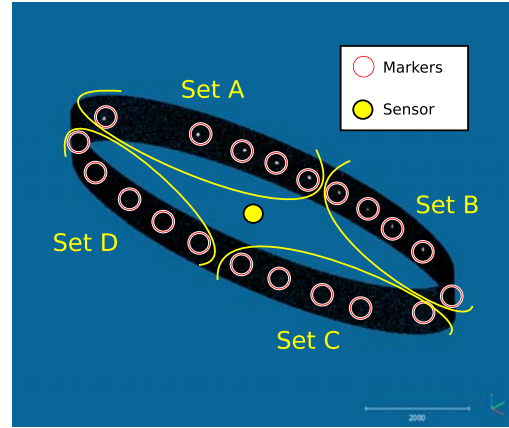

Fig. 4. Simulated environment with targets at different distances from the sensor and different SNRs.

TABLE III
SNR VALUES USED IN THE SIMULATED ENVIRONMENT WITH
TARGETS AT DIFFERENT DISTANCES

Target set	A	B	C	D
SNR	2	10	100	10000

each set are at different distances, such that with respect to the sensor, each target has an apparent size that doubles that of the previous, closer target. Fig. 4 shows this environment. The dark points represent noise or clutter data surrounding the targets, shown as white points. The reflected intensity values of the background noise data points were generated using an exponential distribution. The circled points represent the targets. Their reflected intensity values were generated from a Rayleigh distribution to comply with the CA-CFAR assumptions, as will be justified in Section V-B1. The SNR for each set is listed in Table III.

Fig. 5 shows the ROC curves for the 3-D detectors. The probability of detection (TPR) is plotted against the actual probability of false alarm (FPR), which results from changing the theoretical false alarm parameters ($P_{\text{fa}}^{\text{CA-CFAR}}$ and $P_{\text{fa}}^{\text{OS-CFAR}}$) in the CFAR processors.

In this data set, cacfar3D(Pcd) and oscfar3D(Pcd) exhibit comparable performances, while segmentation thresholding yields a slightly lower performance during most of the ROC curve. The 3-D RANSAC method is unable to declare any detection. In this application, the number of points in the PCD is much larger than the number of inliers required by RANSAC 3-D to detect ellipsoids. This means that even when the maximum number of RANSAC iterations is large, there is a high probability that the 3-D RANSAC method finds a group of points that matches the expected model but corresponds to another, usually significantly larger, structure (ellipsoid) in the PCD. For example, it was observed, in all the experiments, that some planar sections were matched to large ellipsoids. When this occurs, the CCA algorithm discards these detections due to size constraints leaving no or very few detections, and the points in the ROC curve are very close or equal to zero.
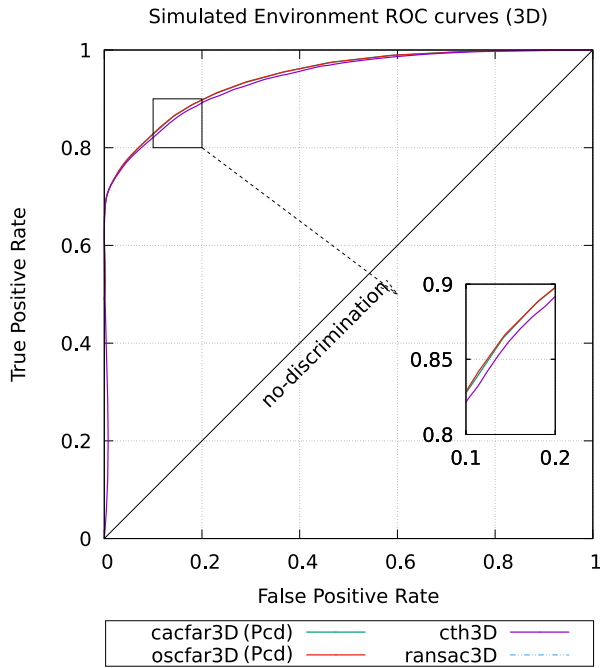
Fig. 5. ROC curves of the methods applied to 3-D PCD in the data set with targets at different distances.
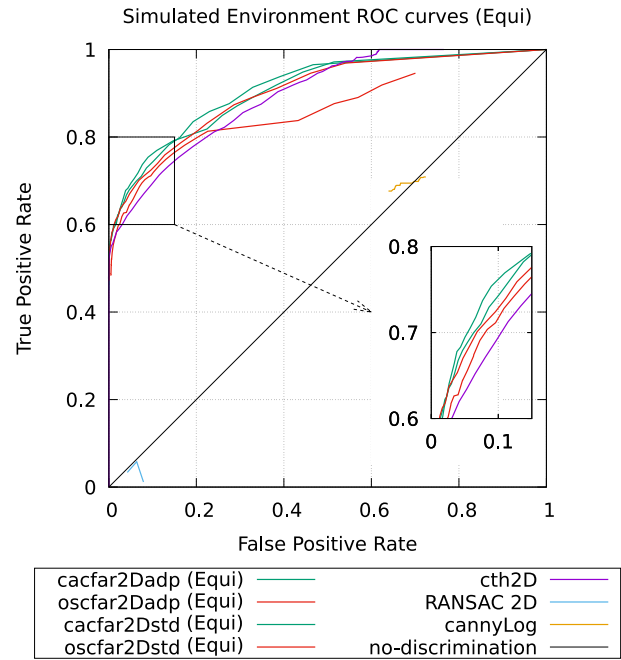

Fig. 6. ROC curves of the methods applied to the equirectangular 2-D projected data set with targets at different distances.

TABLE IV
RANK (R) OF 3-D AND 2-D METHODS BASED ON
ROC CURVES FOR FPR ≤ 0.15

R	3D	2D Equi.	2D Merc.
1	cacfar3D(Pcd)	cacfar2Dadp	cacfar2Dadp
2	oscfar3d(Pcd)	cacfar2Dstd	cacfar2Dstd
3	cth3D	oscfar2Dstd	oscfar2Dstd
4	ransac3D	oscfar2Dadp	oscfar2Dadp
5		cth2D	cth2D
6		RANSAC 2D	RANSAC 2D
7		cannyLog	cannyLog

Fig. 7. ROC curves of the methods applied to the Mercator 2-D projected data set with targets at different distances.

Although, with the exception of RANSAC 3-D, there is little difference in the ROC curves for the 3-D algorithms, this simulated data set is particularly useful for assessing the performance of the proposed 2-D adaptive window size versions of the CFAR methods. This is because the standard 2-D CFAR methods are sensitive to the target size, which is used to define the guard cells' window size parameter. ROC curves for the equirectangular and Mercator 2-D projected data are shown in Figs. 6 and 7, respectively. For this data set, both 2-D projections ("Equi" and "Merc") show comparable results.

Table IV gives each 3-D and 2-D method a rank R based on the ROC performances for values of FPR ≤ 0.15. The rankings R in Table IV results from the average TPR value (highest to lowest) over the FPR interval considered ($0 \leq$ FPR ≤ 0.15). Note that it is at low FPR values that each CFAR processor is challenged in producing a high TPR, and therefore, the performances are compared at these FPR values. Note the poor performance of RANSAC 2-D. As in
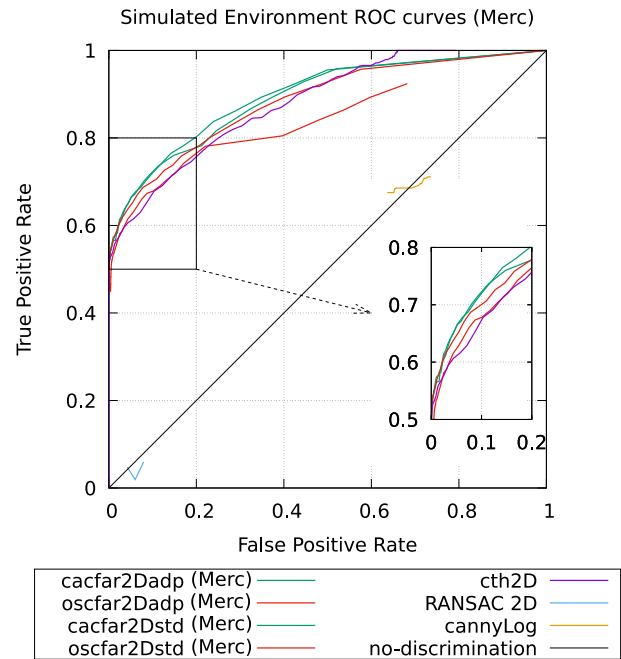
the case of 3-D RANSAC, this is again due to multiple points in each image contributing to structures (in this case, ellipses) that are much larger than the actual markers.

Note that the adaptive CA-CFAR methods outperform all other 2-D methods, including the adaptive OS-CFAR processor. This can be explained by the fact that unlike the CA-CFAR processor, the OS-CFAR processor does not assume additive noise but rather multiplicative noise. In the simulations used so far, the noise and target noise sources have been generated
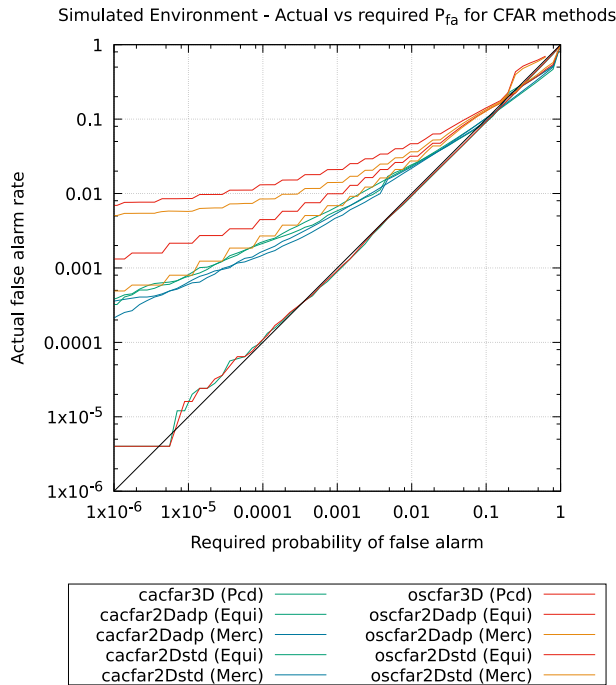
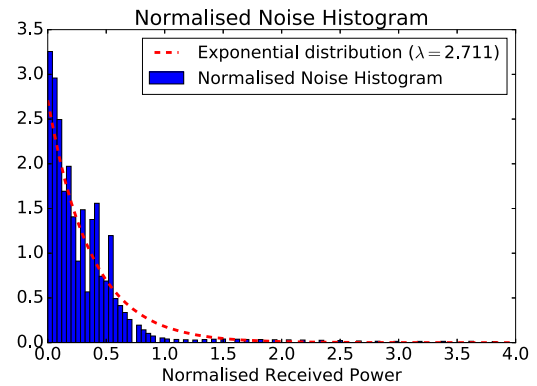Fig. 8. Probability of false alarm versus required FAR in data set with targets at different distances.

Fig. 9. Received power clutter histogram from an indoor laboratory environment.

Fig. 10. Received power clutter histogram in an underground mine environment.

in an additive manner, with exponential and Rayleigh distributions, respectively, so that the CA-CFAR assumptions are met.

Fig. 8 plots all of the CFAR methods' actual FARs versus the theoretical probability of false alarm parameter used in the CFAR algorithms. It can be observed that both 3-D versions of the CFAR methods [cacfar3D(Pcd) and oscfar3D(Pcd)] present the best performance with respect to both probability of detection (see Fig. 5) and achieving the desired FAR (see Fig. 8). For probability of FARs higher than 10^{-5}, the 3-D OS-CFAR and CA-CFAR algorithms almost perfectly achieve the desired FARs, while maintaining the highest detection rates.

In relation to the 2-D projections used, the equirectangular projection introduces a higher[5] distortion in the shape of the markers. In the case of the CA-CFAR methods, the adaptive version is, thus, capable of presenting a higher TPR than the standard version at low FPR values.

In all cases, the adaptive OS-CFAR detector exhibits the lowest TPR values among the CFAR methods. Due to the CA-CFAR assumptions used in generating the data, the OS-CFAR is not the optimal CFAR detector. It is also interesting to note, however, that the adaptive window size of the 2-D adaptive OS-CFAR processor (oscfar2Dadp) sometimes contained insufficient data points, thus negatively impacting the OS reference power estimate.

Regarding the benchmark methods, 2-D RANSAC (RANSAC 2-D) yields very low TPR values and only in a limited FPR range. The Canny detector (CannyLog) behaves in a similar way, but all its ROC curve points correspond

to high FPR values and are, therefore, not considered in the ranking table. The segmentation thresholding method (cth2D) is ranked below all the CFAR methods.

B. Results With Real Data

An indoor laboratory environment and an underground mine are used for comparing the 3-D PCD and 2-D projected image marker detection algorithms with real data. Before applying the CFAR methods to real ladar data, it is useful to check whether the assumptions for the validity of the CFAR algorithms are approximately obeyed, the most important of them is the noise and target distribution types.

1) Ladar Target Noise Distributions: Ladar data captured in the two environments are used to determine the corresponding clutter and target distributions. The received power intensity values of points where there are no markers are used to obtain clutter distributions (see Figs. 9 and 10), while points corresponding to markers are used to determine typical target distributions. Fig. 11 shows an example target distribution.[6] In each figure, the blue discrete data represents the sample distributions, and the red curves represent their best fit continuous distributions. In the case of noise

---

[5]Note that the diameter rather than the radius of the markers was used to set the guard window size, since the CUT could lie on or near the circumference of a marker. hence $Rgc = aRT$, with $a = 2$.

[6]Note that the reflectance values recorded by the sensor used in the experiments (Riegl VZ-400) correspond to a reflected intensity relative to the intensity of a white diffuse target at the same distance; thus, the reflected intensity values are unitless. The sensor stores these values in dB. The linear reflectance is calculated from the logarithmic values.
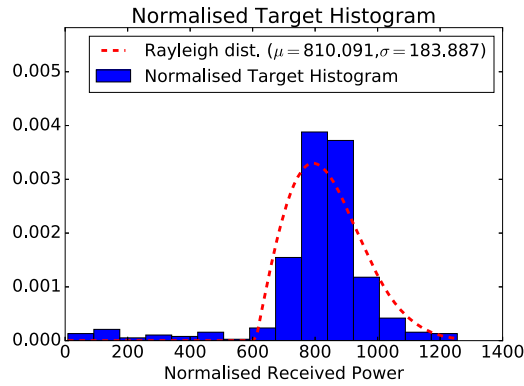
Fig. 11.   Received power target histogram in an indoor environment.

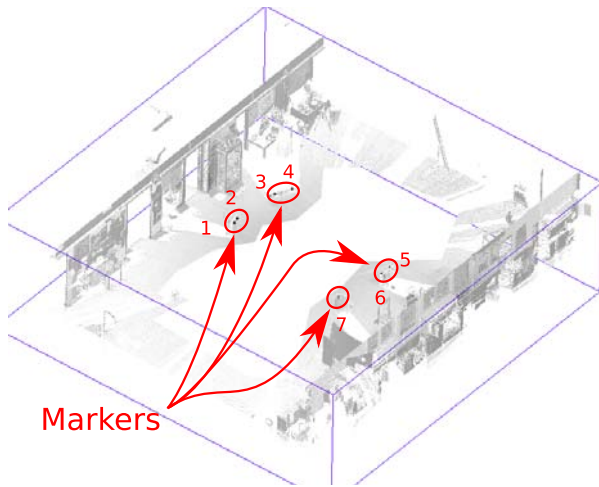| R	3D	Equi.	Merc.
1	oscfar3D(Pcd)	oscfar2Dadp	oscfar2Dadp
2	cacfar3D(Pcd)	oscfar2Dstd	oscfar2Dstd
3	cth3D	cacfar2Dadp	cacfar2Dadp
4	ransac3D	cacfar2Dstd	cacfar2Dstd
5		cth2D	cth2D
6		cannyLog	cannyLog
7		RANSAC 2D	RANSAC 2D

Fig. 12.   Indoor laboratory environment. Darker points: higher reflected logarithmic intensity.

(see Figs. 9 and 10), exponential distributions were fit, and for the target (see Fig. 11), a Rayleigh distribution was fit.

Note that CA and OS-CFAR processors assume the form of an exponential noise/clutter distribution but make no assumptions on the exponential distribution parameter itself, which would differ for Figs. 9 and 10. The Rayleigh target statistics are also assumed in the derivation of the detection statistics of the CA-CFAR detector, and therefore, Fig. 11 together with Figs. 9 and 10 at least approximately justify the use of CA-CFAR processors in these environments [29].

2) Results (Indoor Laboratory Environment): Fig. 12 shows 3-D PCD recorded in the laboratory environment, which contains seven reflective markers to be detected. Darker points represent a higher reflected intensity on a logarithmic scale. For ground-truth comparison purposes, the reflective markers were identified manually within the 3-D PCD along with their corresponding pixels in the 2-D projected images (see Figs. 13 and 14).[7] The environment includes objects (clutter) that yield intensity values close to those of the targets.

[7]Note that in Figs. 12–14, PCD corresponding to the laboratory ceiling has been manually removed for visual purposes. All detection algorithms, however, used the complete PCD.

The CFAR parameters in this experiment were the same as in the simulation since the targets were of similar size.

For comparison purposes, it was necessary to challenge the detectors by adding artificial clutter to the indoor environmental data. This was achieved by adding 0.2% of the total number of points, corresponding to two false alarms per every 1000 laser PCD measurements. This corresponds to an increase in the number of highly reflective, nonmarker points/objects, which would degrade the performance of the various detectors. In Section V-B3, an underground mine environment is used, which contains dust and naturally occurring patches of reflective material on its walls, providing a challenging scenario for the detectors in terms of clutter and the potential for missed detections.

The ROC curves for the methods applied directly to the 3-D PCD data set from the indoor laboratory environment are shown in Fig. 15, where, to demonstrate each detector's performance at low FPRs, a logarithmic FPR axis is used. Note that compared to the 3-D CFAR algorithms, the segmentation thresholding method (cth3D) results in a decreased TPR, for FARs below 0.2% as expected. Once again, 3-D RANSAC failed to make successful detections.

Figs. 16 and 17 present ROC curves obtained from 2-D data using the equirectangular and Mercator projections, respectively. Comparing Fig. 15 with Figs. 16 and 17 shows that the 2-D versions of the algorithm present lower performances than 3-D versions with probabilities of detection ranging between 50% and 70% for $2 \times 10^{-4} \leq$ FPR ≤ 0.1. Table V again ranks each 3-D and 2-D method based on average TPR performance for values of FPR ≤ 0.1. In this environment, the 3-D and adaptive 2-D OS-CFAR detectors (oscfar3D(Pcd) and oscfar2Dadp) give the best performances. Also, the adaptive 2-D CA-CFAR versions perform better than their standard counterparts. Both, adaptive and standard, OS-CFAR versions showed a better performance than the segmentation thresholding method. As in the results with 3-D PCD, the CA-CFAR methods yielded a slightly lower performance than the OS-CFAR methods.

For FPR values below 0.002, the effect of the artificially introduced clutter is more noticeable, negatively affecting the performance of both the 2-D and 3-D segmentation thresholding methods (cth3D and cth2D) while affecting the 2-D and 3-D CA-CFAR methods to a much lesser extent.

Fig. 13.   Mercator projected image of indoor laboratory environment.

Fig. 14.   Equirectangular projected image of indoor laboratory environment.
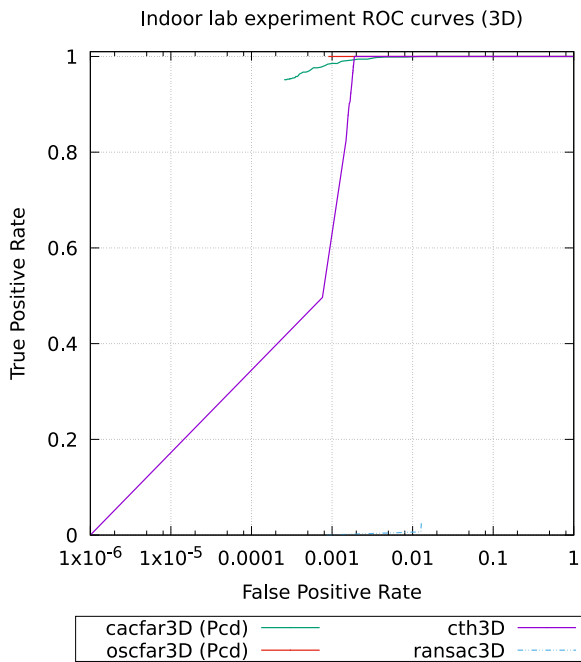

Fig. 15.   ROC curves of the methods applied to 3-D PCD in the indoor laboratory experimental data set.
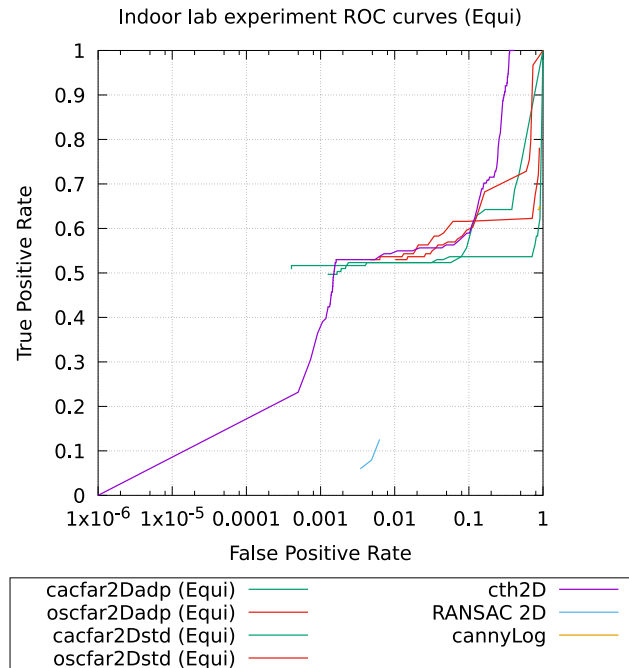

Fig. 16.   ROC curves of the methods applied to equirectangular 2-D projected data in the indoor laboratory experimental data set.

Again the problem with the standard and adaptive 2-D OS-CFAR processors (oscfar2Dstd and oscfar2Dadp) was observed, as insufficient data points were captured in the reference cell windows to produce a useful OS at FPR < 0.01. However, for FPR > 0.01, the 2-D OS-CFAR detectors show superior TPRs than the 2-D CA-CFAR detectors. This can be explained due to the real data itself not complying with the CA-CFAR statistical assumptions. The other benchmark methods, 2-D RANSAC and the Canny detector, exhibit similar problems to those shown with the simulated data.

The actual FAR versus the chosen theoretical FAR parameter is shown in Fig. 18. In terms of the actual FAR, all methods present a poor performance when the chosen FAR parameter values were below 1×10^{-3}, with 3-D CA-CFAR [cacfar3D(Pcd)] performing best. Note that for required probabilities of false alarm between 0.001 and 0.4, the cacfar3D(Pcd) detector produces actual FARs that are even lower than the set value.

3) Results (Mine Environment): Finally, a data set obtained in an underground mine was also used to test the algorithms.

As shown in Fig. 19, the data set contains a large number of points with seven markers, five of them are in the tunnel (red circles) and two of them are located on the end wall (green circles). To provide a real and challenging scenario, comparisons were made in the presence of dust, thus increasing the clutter level for each detection algorithm.

Fig. 20 shows the ROC curves of the 3-D detectors applied directly to the 3-D PCD. Similar behavior to that observed in the indoor laboratory data set is noted. The 3-D CFAR methods are least affected by the high level of clutter, while the constant thresholding method (cth3D) shows a decreased true positive detection rate for FARs below 0.025. The CA-CFAR processor [cacfar3D(Pcd)], however, generally gives a much lower probability of detection than the other methods (near 70% for most values of FPR). Although the clutter histogram generated in Fig. 10 does approximately satisfy the CA-CFAR assumptions, the local statistics in the CA-CFAR window may not, meaning that the noise distribution assumptions are not always met within the CA-CFAR noise window. In contrast, the 3-D OS-CFAR processor yields a very high detection rate
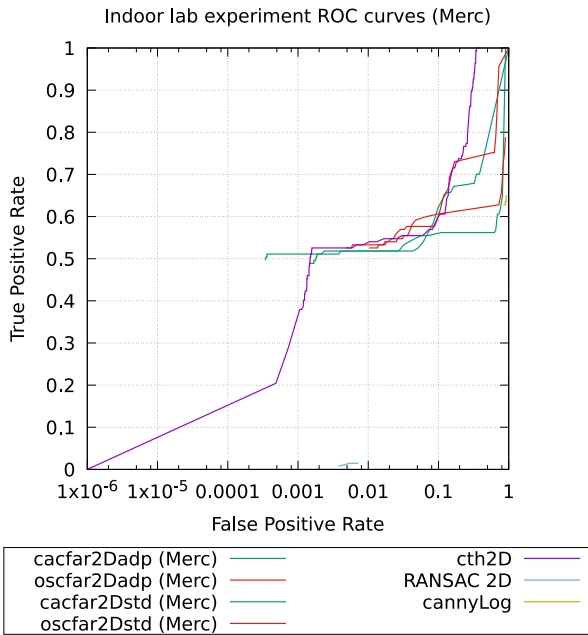
Fig. 17. ROC curves of the methods applied to the Mercator 2-D projected data in the indoor laboratory experimental data set.
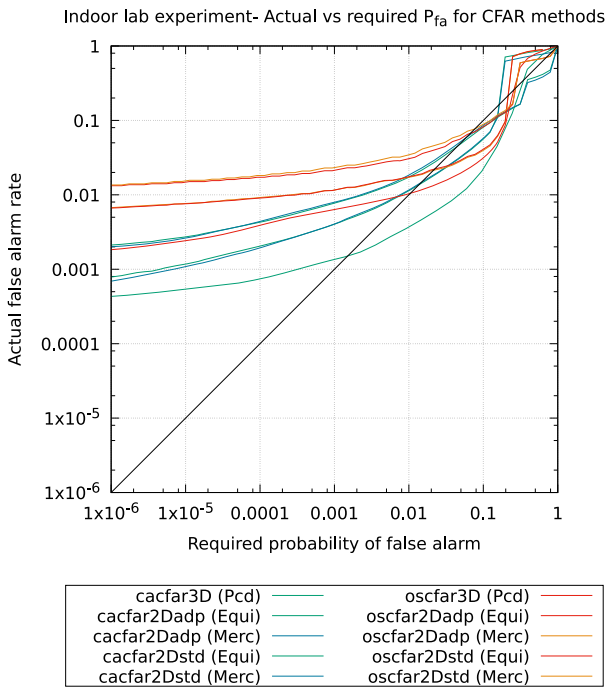

Fig. 18. Probability of false alarm versus required FAR for indoor laboratory data (artificial clutter).

at low probabilities of false alarm. This can be attributed to its more realistic noise distribution assumptions.

ROC curves for the 2-D equirectangular and Mercator projected data are shown in Figs. 21 and 22, respectively. Table VI ranks each 3-D and 2-D method based on average TPR performance for values of FPR $\leq$ 0.1. It can be seen that the constant threshold detector (cth2D) shows a decreased true positive detection rate for FARs below 0.008. Note that it
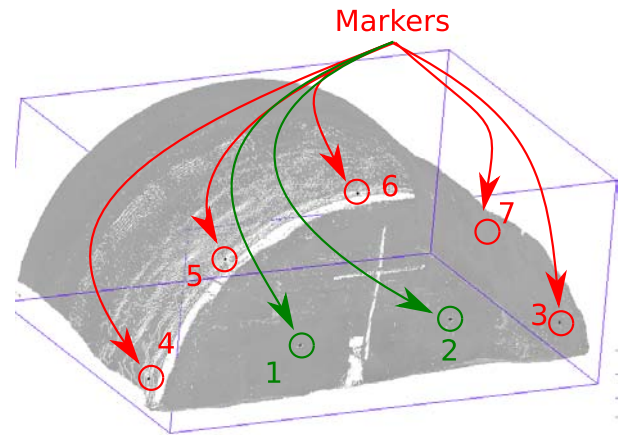

Fig. 19. Section of an underground mine tunnel. Red and green circles: visible targets' locations.
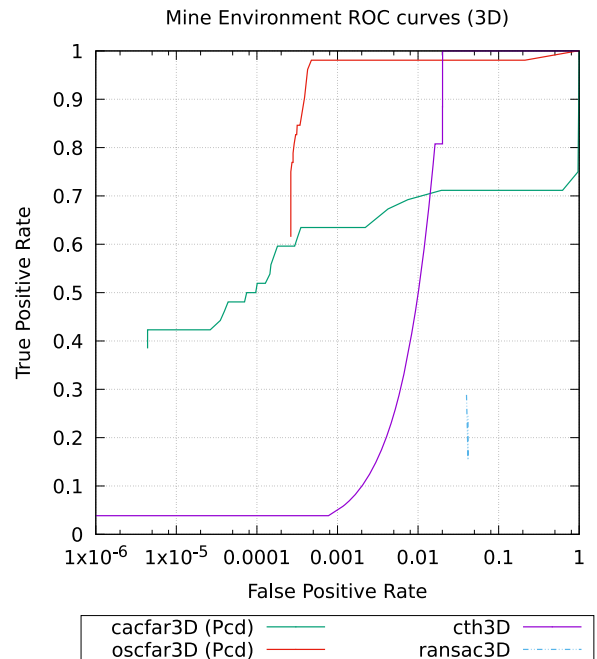

Fig. 20. ROC curves of the methods applied to 3-D PCD in the underground mine tunnel data set in the presence of dust.

TABLE VI
RANKING OF 2-D METHODS, APPLIED TO THE MINE DATA SET, BASED ON ROC CURVES FOR FPR < 0.1

R	3D	Equi.	Merc.
1	oscfar3D(Pcd)	cacfar2Dstd	cacfar2Dadp
2	cacfar3D(Pcd)	cacfar2Dadp	cacfar2Dstd
3	cth3D	cth2D	cth2D
4	ransac3D	oscfar2Dstd	oscfar2Dadp
5		oscfar2Dadp	oscfar2Dstd
6		RANSAC 2D	RANSAC 2D
7		cannyLog	cannyLog

is only under the 2-D Mercator projection that the adaptive versions of both the CA-CFAR and OS-CFAR processors
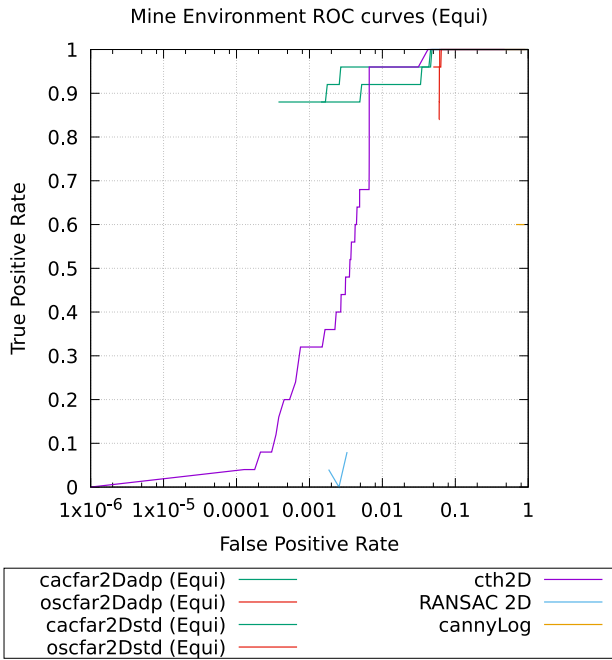
Fig. 21. ROC curves of the methods applied to equirectangular 2-D projected data in the underground mine tunnel data set.
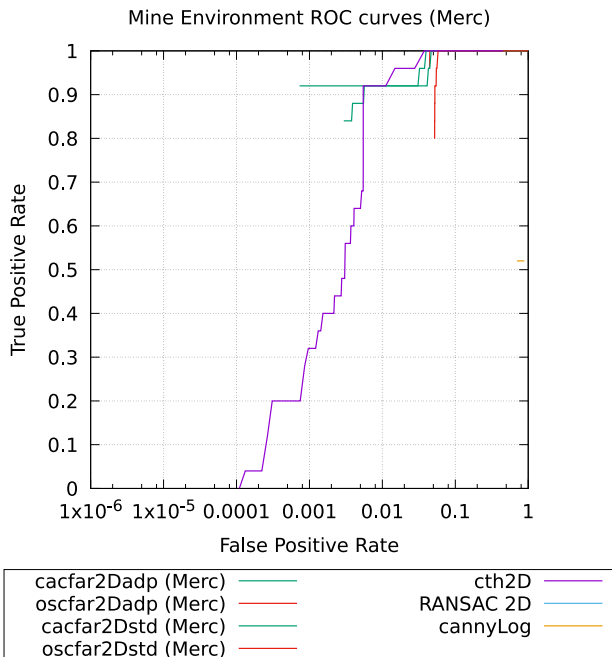

Fig. 22. ROC curves of the methods applied to the Mercator 2-D projected data in the underground mine tunnel data set.

(cacfar2Dadp and oscfar2Dadp) slightly outperform their state-of-the-art fixed window size counterparts (cacfar2Dstd and oscfar2Dstd). This can be attributed to the equirectangular projection introducing more distortion in the shape of the markers.

Under the equirectangular projection, for FPR < 0.05, the adaptive CA-CFAR detector (cacfar2Dadp) yielded lower TPR values than its standard counterpart (cacfar2Dstd). This can also be explained since the adaptive window does not include enough points to obtain a good estimate of the clutter power level. In this particular data set, this is due to the targets
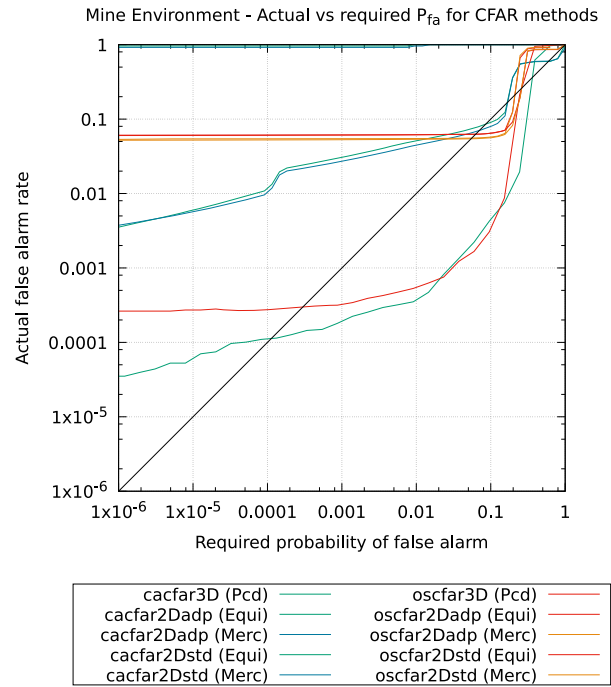

Fig. 23. Probability of false alarm versus required FAR for the underground mine tunnel data.

being far from the sensor, thus exhibiting a small apparent size that left very few pixels available to calculate the size of the reference window. For FPR > 0.08, all 2-D detectors produced comparable performances.

Fig. 23 shows the actual probability of false alarm curves versus the chosen, theoretical probability of false alarm parameter used by each detector. The 3-D CFAR methods [cacfar3D(Pcd) and oscfar3D(Pcd)] present the best performances by achieving even lower actual FARs than the set FARs for values above 5×10^{-4} and below 0.3. All the 2-D OS-CFAR methods present a similar performance as do the 2-D adaptive CA-CFAR detectors for both the Mercator and equirectangular projections.

Overall, the 3-D OS-CFAR detector is the only method showing a very high detection probability (greater than 96%) over a large range of FPRs (see Fig. 20), which simultaneously gives an actual FAR similar or below the required value (see Fig. 23).

VI. CONCLUSION

There are various conclusions that can be drawn from the simulated experiments, which are directly applicable to all of the real experimental results. These are given as conclusions 1-4 in the following. However, certain conclusions that can be drawn from the simulated results only partially apply to the real results. These are given as conclusions 5-7 in the following, together with the suggested explanations of the differences. Finally, conclusions 8 and 9 provide suggestions regarding the appropriate circumstances under which the adaptive 2-D CFAR processors and the OS-CFAR processors should be used.

1) In all of the experiments, the proposed 3-D CFAR detectors [cacfar3D(Pcd) and oscfar3d(Pcd)] outperformed

the benchmark 3-D RANSAC and constant threshold detectors (see Tables IV–VI). Their advantages are particularly apparent in Figs. 8, 18, and 23, as the actual FPR is similar to, or even less than, the desired CFAR FPR.

2) The 3-D CFAR algorithms exhibit better performance than their 2-D CFAR counterparts as there is no distortion in the size or shape of the markers.

3) The Canny edge detector yielded low TPRs even at higher FPRs, as observed with both simulated and real data.

4) The RANSAC method also yielded a low performance in its 2-D form, while the spatial data structure in 3-D also negatively affected its performance, as several different structures were consistent with the elliptical model, and falsely detected. It should be noted, however, that RANSAC could be used after the detection phase to check whether the detected objects match a particular shape and size.

5) The proposed adaptive window 2-D CA-CFAR detector outperformed its standard counterpart in all experiments, except in the mine using the equirectangular projection, where a slight degradation could be seen over a small interval of FPRs. This can be attributed to the distortion introduced by the equirectangular projection. Note that the adaptive version gives superior performance when the Mercator projection is used since this projection introduces less distortion of the data.

6) The proposed adaptive window 2-D OS-CFAR detector (oscfar2Dadp) again outperformed its standard counterpart in the laboratory environment and under the Mercator projection of the mine data. Once again, it is suggested that the slight degradation in its performance with the equirectangular projection of the mine data (see Table VI) is due to the distortion of the data. In the simulated data, a small degradation was also evident (see Table IV) due to the CA-CFAR statistical assumptions used in generating the simulated data.

7) In the simulated experiments, in which the noise and target distributions obeyed the CA-CFAR assumptions, and for targets that gave high SNRs, the proposed 2-D CFAR methods yielded comparable performances with the state-of-the-art detection methods (see Figs. 5–8).

8) With 2-D data, and if it is known that the targets have very different apparent sizes, the adaptive window size CFAR versions should be used. Else, when the apparent sizes of the targets do not vary significantly, the standard versions should be used due to their lower computational complexity.

9) The adaptive OS-CFAR processor should be used when it is expected that some of the points representing the target will spread into the reference cell window (i.e., when detecting large objects).

REFERENCES

[1] P. J. Besl and D. N. McKay, "A method for registration of 3-D shapes," *IEEE Trans. Pattern Anal. Mach. Intell.*, vol. 14, no. 2, pp. 239–256, Feb. 1992.

[2] M. Hebel and U. Stilla, "Simultaneous calibration of ALS systems and alignment of multiview LiDAR scans of urban areas," *IEEE Trans. Geosci. Remote Sens.*, vol. 50, no. 6, pp. 2364–2379, Jun. 2012.

[3] D. G. Lowe, "Distinctive image features from scale-invariant keypoints," *Int. J. Comput. Vis.*, vol. 60, no. 2, pp. 91–110, 2004.

[4] H. Bay, A. Ess, T. Tuytelaars, and L. Van Gool, "Speeded-up robust features (SURF)," *Comput. Vis. Image Understand.*, vol. 110, no. 3, pp. 346–359, 2008.

[5] E. Rublee, V. Rabaud, K. Konolige, and G. Bradski, "ORB: An efficient alternative to SIFT or SURF," in *Proc. IEEE Int. Conf. Comput.*, Nov. 2011, pp. 2564–2571.

[6] S. van der Walt *et al.*, "Scikit-image: Image processing in Python," *PeerJ*, vol. 2, p. e453, Jun. 2014, doi: 10.7717/peerj.453.

[7] J. Canny, "A computational approach to edge detection," *IEEE Trans. Pattern Anal. Mach. Intell.*, vol. PAMI-8, no. 6, pp. 679–698, Nov. 1986.

[8] M. A. Fischler and R. Bolles, "Random sample consensus: A paradigm for model fitting with applications to image analysis and automated cartography," *Commun. ACM*, vol. 24, no. 6, pp. 381–395, 1981, doi: 10.1145/358669.358692.

[9] A. Nurunnabi, D. Belton, and G. West, "Robust segmentation for large volumes of laser scanning three-dimensional point cloud data," *IEEE Trans. Geosci. Remote Sens.*, vol. 54, no. 8, pp. 4790–4805, Aug. 2016.

[10] N. J. Mitra and A. Nguyen, "Estimating surface normals in noisy point cloud data," in *Proc. 19th Annu. Symp. Comput. Geometry*, Jun. 2003, pp. 322–328.

[11] P. Hansen, P. Corke, W. Boles, and K. Daniilidis, "Scale-invariant features on the sphere," in *Proc. IEEE 11th Int. Conf. Comput. Vis.*, Oct. 2007, pp. 1–8.

[12] P. Hansen, P. Corke, W. Boles, and K. Daniilidis, "Scale invariant feature matching with wide angle images," in *Proc. IEEE/RSJ Int. Conf. Intell. Robots Syst.*, Oct./Nov. 2007, pp. 1689–1694.

[13] Y. Yu, J. Li, H. Guan, C. Wang, and J. Yu, "Semiautomated extraction of street light poles from mobile LiDAR point-clouds," *IEEE Trans. Geosci. Remote Sens.*, vol. 53, no. 3, pp. 1374–1386, Mar. 2015.

[14] X. Liang *et al.*, "Terrestrial laser scanning in forest inventories," *ISPRS J. Photogramm. Remote Sens.*, vol. 115, pp. 63–77, May 2016.

[15] M. Fiala, "Designing highly reliable fiducial markers," *IEEE Trans. Pattern Anal. Mach. Intell.*, vol. 32, no. 7, pp. 1317–1324, Jul. 2010.

[16] T. Nakamura and S. Suzuki, "Simplified SLAM using reflection intensity of laser range sensor with retro-reflective marker," in *Proc. SICE Annu. Conf. (SICE)*, Aug. 2012, pp. 2074–2079.

[17] D. S. Kalpoe, "Vibration measurement of a model wind turbine using high speed photogrammetry," M.S. thesis, Dept. Geosci. Remote Sens., Delft Univ. Technol., Delft, The Netherlands, Nov. 2010.

[18] J. Schou, H. Skriver, A. A. Nielsen, and K. Conradsen, "CFAR edge detector for polarimetric SAR images," *IEEE Trans. Geosci. Remote Sens.*, vol. 41, no. 1, pp. 20–32, Jan. 2003.

[19] D. Tao, S. N. Anfinsen, and C. Brekke, "Robust CFAR detector based on truncated statistics in multiple-target situations," *IEEE Trans. Geosci. Remote Sens.*, vol. 54, no. 1, pp. 117–134, Jan. 2016.

[20] D. Tao, A. P. Doulgeris, and C. Brekke, "A segmentation-based CFAR detection algorithm using truncated statistics," *IEEE Trans. Geosci. Remote Sens.*, vol. 54, no. 5, pp. 2887–2898, May 2016.

[21] I. Saban and S. Faibish, "Image processing techniques for laser images," in *Proc. Can. Conf. Elect. Comput. Eng.*, 1996, pp. 462–465.

[22] F. Zhang, C. Li, and L. Shi, "Detecting and tracking dim moving point target in IR image sequence," *Infr. Phys. Technol.*, vol. 46, no. 4, pp. 323–328, Apr. 2005.

[23] H. Rohling, "Radar CFAR thresholding in clutter and multiple target situations," *IEEE Trans. Aerosp. Electron. Syst.*, vol. 19, no. 4, pp. 608–621, Jul. 1983.

[24] L. G. Shapiro and G. C. Stockman, *Computer Vision* (Binary Image Analysis). Upper Saddle River, NJ, USA: Prentice-Hall, 2002, ch. 3, pp. 69–73.

[25] A. Foessel, J. Bares, and W. R. L. Whittaker, "Three-dimensional map building with MMW radar," in *Proc. 3rd Int. Conf. Field Service Robot.*, Helsinki, Finland, Jun. 2001, pp. 1–6.

[26] D. Langer, "An integrated MMW radar system for outdoor navigation," in *Proc. IEEE Int. Conf. Robot. Automat.*, Minneapolis, MN, USA, Apr. 1996, pp. 417–422.

[27] M. Barkat, *Signal Detection and Estimation*. Norwood, MA, USA: Artech House, 2005. [Online]. Available: http://books.google.com/books?id=Le5SAAAAMAAJ

[28] D. R. Morgan, "Two-dimensional normalization techniques," *IEEE J. Ocean. Eng.*, vol. 12, no. 1, pp. 130–142, Jan. 1987.

[29] M. Adams, J. Mullane, E. Jose, and B.-N. Vo, *Robotic Navigation and Mapping with Radar*. Norwood, MA, USA: Artech House, 2012. [Online]. Available: https://books.google.cl/books?id=4sw8IpAjhvsC

[30] H. Houshiar, J. Elseberg, D. Borrmann, and A. Nüchter, "A study of projections for key point based registration of panoramic terrestrial 3D laser scan," *Geo-Spatial Inf. Sci.*, vol. 18, no. 1, pp. 11–31, 2013.

[31] K. Rosen, *Discrete Mathematics and Its Applications* (Discrete Mathematics and Its Applications). New York, NY, USA: McGraw-Hill, 2007. [Online]. Available: https://books.google.cl/books?id=ZYZfQgAACAAJ

[32] J. L. Bentley, "Multidimensional binary search trees used for associative searching," *Commun. ACM*, vol. 18, no. 9, pp. 509–517, 1975, doi: 10.1145/361002.361007.

[33] S. Maneewongvatana and D. M. Mount, "It's okay to be skinny, if your friends are fat," in *Proc. Center Geometric Comput. 4th Annu. Workshop Comput. Geometry*, vol. 2, 1999, pp. 1–8.

[34] R. Schnabel, R. Wahl, and R. Klein, "Efficient ransac for point-cloud shape detection," *Comput. Graph. Forum*, vol. 26, no. 2, pp. 214–226, Jun. 2007.

[35] OpenCV Team. (Dec. 18, 2015). *Open Source Computer Vision: Canny Edge Detection*. Accessed: May 24, 2018. [Online]. Available: https://docs.opencv.org/3.1.0/da/d22/tutorial_py_canny.html

Hamidreza Houshiar received the bachelor's degree in information technology, the master's degree in smart systems, and the Dr.rer.nat. degree in computer science from the University of Würzburg, Würzburg, Germany, in 2009, 2011, and 2017, respectively.

He was with Islamic Azad University, South Branch, Tehran, Iran, Jacobs University Bremen, Bremen, Germany, and the University of Würzburg. He is currently a Software Engineer with Blickfeld GmbH, Munich, Germany. He works on LiDAR technology, point cloud processing, autonomous vehicles, computer vision, and robotics. His research interests include scene recognition, 3-D environment mapping, and object tracking.

Daniel Lühr (S'99–M'04–SM'19) was born in Santiago, Chile, in December 1978. He received the Lic.Sci. and the Dipl. degrees in electrical engineering and the Ph.D. degree from the Universidad de Chile, Santiago, in 2003, 2004, and 2018, respectively.

From 2004 to 2006, he was a Research Associate and a no-fee Consultant to the Submilimeter Receiver Laboratory, Harvard-Smithsonian Center for Astrophysics, Cambridge, MA, USA. From 2007 to 2009, he was an Adjoint Professor with the Universidad Austral de Chile, Valdivia, Chile. From 2009 to 2013, he was Consultant to the Chilean Ministry of Energy. He is currently with the Facultad de Ciencias de la Ingeniería, Institute of Electricity and Electronics, Universidad Austral de Chile. He has expertise in digital systems, system integration, medical devices, and robotics. His research interests include robotics and engineering applications in astronomy (astroengineering).

Dorit Borrmann received the bachelor's degree in computer science and mathematics and the master's degree in computer science from Osnabrück University, Osnabrück, Germany, in 2006 and 2009, respectively, and the Dr.rer.nat. degree from the University of Würzburg, Würzburg, Germany, in 2018.

She was with Jacobs University Bremen, Bremen, Germany, the Rochester Institute of Technology, Rochester, NY, USA, and Osnabrück University. She is currently a Post-Doctoral Researcher with the Robotics and Telematics Group, University of Würzburg. Her research interests include autonomous mobile robots, 3-D environment mapping, laser scanning technologies, and 3-D thermal modeling.

Martin Adams (SM'08) received the degree in engineering science from the University of Oxford, Oxford, U.K., in 1988, and the D.Phil. degree from the Robotics Research Group, University of Oxford, in 1992.

He continued his research in autonomous robot navigation as a Project Leader and a part-time Lecturer at the Institute of Robotics, Swiss Federal Institute of Technology (ETH), Zürich, Switzerland. He was a Guest Professor and taught control theory at St. Gallen, Switzerland, from 1994 to 1995. From 1996 to 2000, he was a Senior Research Scientist in robotics and control and the field of semiconductor assembly automation with the European Semiconductor Equipment Centre (ESEC), Steinhausen, Switzerland. From 2000 to 2010, he was an Associate Professor with the School of Electrical and Electronic Engineering, Nanyang Technological University (NTU), Singapore. He is currently a Professor of electrical engineering with the Department of Electrical Engineering, University of Chile, Santiago, Chile. He is also a Principle Investigator with the industrially sponsored Advanced Mining Technology Center (AMTC), Santiago. His research interests include autonomous robot navigation, space situational awareness, sensing, and sensor data interpretation and control. He has published many technical articles in these fields.

Dr. Adams has been a Principle Investigator and the leader of many robotics and industrially sponsored projects, coordinating researchers from local industries and local and overseas universities, and has served as an Associate Editor for various journal and conference editorial boards. He is also the Chair of the IEEE Robotics and Automation Society, Chilean Chapter.

Andreas Nüchter (M'99) received the Diploma degree in computer science and the Dr.rer.nat degree from University of Bonn, Bonn, Germany, in 2006.

He was with Jacobs University Bremen, Bremen, Germany, Osnabrück University, Osnabrück, Germany, the Fraunhofer Institute for Autonomous Intelligent Systems (AIS), Sankt Augustin, Germany, the University of Bonn, and Washington State University, Pullman, WA, USA. He is currently a Professor of computer science (telematics) with the University of Würzburg, Würzburg, Germany. He works on robotics and automation, cognitive systems, and artificial intelligence. His current research interests include reliable robot control, 3-D environment mapping, 3-D vision, and laser scanning technologies.

Dr. Nüchter is also a member of the German Society of Informatics (GI). His thesis was shortlisted for the EURON Ph.D. Award. He received the Best Paper Award from GI for his thesis.